Tribol Lett (2011) 44:139–149
DOI 10.1007/s11249-011-9831-5

ORIGINAL PAPER

Relationship Between Physical Structure and Tribology of Single Soot Particles Generated by Burning Ethylene

Hiralal Bhowmick · S. K. Biswas

Received: 23 December 2010 / Accepted: 20 July 2011 / Published online: 21 August 2011

Abstract Ethylene gas is burnt and the soot generated is sampled thermophoretically at different heights along the flame axis starting from a region close to the root of the flame. The morphology and crystallinity of the particle are recorded using high resolution transmission electron microscopes. The hardness of a single particle is measured using a nanoindenter. The frictional resistance and material removal of a particle are measured using an atomic force microscope. The particles present in the mid-flame region are found to have a crystalline shell. The ones at the flame root are found to be highly disordered and the ones at the flame tip and above have randomly distributed pockets of short range order. The physical state of a particle is found to relate, but not very strongly, with the mechanical and tribological properties of the particles.

Keywords Single particle · Carbon · Soot structure · Friction · Wear · Hardness · TEM

1 Introduction

At the present level of automobile technology, emission of soot from combustion in diesel engines appears to be an inevitability. Engine soot have been recognized to contribute to the wear of engine components; cylinder and cam tappet assembly. Considering that internal combustion engines play such an important role in industry investigative research of the parametric influences of particle size, agglomeration, oil viscosity, additives, surfactant as well as chemistry and electrical properties of particles on wear as well as into the wear mechanism have not perhaps been as extensive as it is deserved.

It is generally held [1–26] that the presence of soot particles in a zone of tribological contact is responsible for an enhanced wear of the mating surfaces. Investigations have been done examining real engine components where the soot is present in base oils which carry dispersants, detergents, anti-wear additives, friction modifiers and EP additives. A number of works have also been reported where different tribometric contacts [1–8], which used engine oil soot [9, 10] as well as soots suspended in a variety of solvents with and without additives [8, 11, 12], have been examined to investigate different mechanisms which may be held responsible for this enhancement of wear. Based on these studies it emerges that the wear may be related principally to abrasion [1, 2, 8, 13–17] of a softer component by the harder soot particles. Some workers have also reported wear by adhesion [10, 12] and by a polishing mechanism [6, 8]. Soot has been reported to embed on the mating surfaces by mechanical indentation [8] or a chemical mechanism [5, 8, 18–20] where especially the non-graphitic soot etches out the additive induced boundary film to preferentially transport hard soot particle to active sites. This two body abrasion may be modulated by a beneficial enhancement of viscosity [9, 21, 22] and a concomitant increase in the liquid film thickness [21, 22] at contact due to fine soot dispersions in the liquid. The three body effect reduces friction and wear. In real engines the beneficial tribological effects of additive have been suggested [8, 23] to be partially marginalized as they are taken out of action by being chemi-adsorbed on the soot particles [1, 8, 11–13, 24]. An additional contributory factor is geometric. Hindrances related to particle/agglomerate size in the entrainment (contact) zone when the particle size is

H. Bhowmick · S. K. Biswas (✉)
Mechanical Engineering Department, Indian Institute of Science, Bangalore 560012, India
e-mail: skbis@mecheng.iisc.ernet.in

large, may cause liquid lubrication starvation [2, 6, 25, 26] leading to high wear and high friction.

In this complex scenario where many opposed effects, principally observed empirically, combine to make up the aggregate impact of soot on wear there has been a limited emphasis on the structure and morphology of the soot particles as they take part in tribology at contact. Different combustion materials and processes using different fuels are known [23, 27, 28] to generate particles of varying structure, as well as a variety of mechanical and chemical properties. There are some references in previous works [8, 22, 29] to the effects of a priori physical and chemical structures on soot tribology but limited information is available on how such structure relate to mechanical properties and how such structures promote specific aggregations at contact, induced by tribological stresses. We address the latter in our next communication while the present paper focuses on the effect of size, morphology, and crystallography of soot particles on their mechanical strength and frictional properties, as the structure of soot is systematically varied experimentally.

1.1 Previous High Resolution Transmission Electron Microscopy (HRTEM) Studies

The major characterization of the flame soot particles is done by HRTEM and electron diffraction [30–35]. Palotas et al. [30] utilized HRTEM images to extract some of the key structural properties of soot like interplanar spacing, circularity, orientation, elongation, and length distribution of lattice fringes by adopting proper image analysis technique. Zhu et al. [31] analyzed the HRTEM images along with other scanning electron microscope (SEM) and X-ray diffraction (XRD) data to extract the structural information of C_{60}-fullerene. From their analysis they found traces of both graphitic and amorphous carbon in their samples. Chen et al. [32] utilized the HRTEM technique to characterize ultrafine soot aggregates derived from combustion fuels to show the basic structural units of these carbonaceous products to mainly consist of several parallel stacked graphitic layers with interlayer spacing larger than that of pure graphite. Wentzel et al. [33] in their study had combined with HRTEM data numerical simulation to determine fractal properties, particle structure and aerosol dynamics of different soot particles. Using HRTEM characterization technique, Song et al. [34] investigated the dependence of soot nanostructure on the processing conditions employed for soot production. They explored the correlation of soot nanostructure and the oxidative reactivity of the particles with the possible coalescence of heavy polyaromatic hydrocarbons (PAHs) and/or additions of light acetylene blocks. Following their HRTEM investigation, Ishiguro et al. [35] proposed a double structure model of the diesel soot particles. According to them, these are 'primary' spherical particles which join to form chain-like aggregates (secondary particles) in the emitted soot particles. Primary particle has an inner core which is more disordered and amorphous and an outer shell which is more graphitic.

1.2 Present Study

To enable controlled variations of the physical and geometric parameters which define a soot particle a flame is generated in the laboratory by burning ethylene gas and the particles are extracted thermophoretically (see Appendix 1) from different thermal zones of the flame. The laboratory oriented work dictated the choice of a gaseous fuel ethylene to generate the flame. The soot generated from the fuel mainly consists of blocks of acetylene and PAH molecules besides other unsaturated hydrocarbons and polyacetylenes [28]. The particles are characterized by electron diffraction in HRTEM. We measure the hardness of a single soot particle in a nanoindenter and relate the morphological and hardness data to friction and wear we record using an atomic force microscope (AFM).

2 Experimental Details

2.1 Soot Production

In our study for soot formation we used a diffusion flame burner similar to Santoro burner [36]. A customized equipment (Ducom Pvt. Ltd.) was built to generate soot and to collect samples thermophoretically [37–43]. A 7.5 cm diffusion flame is made by combusting an ethylene fuel and air mixture in a modified version of the Sontoro burner [36]. In diesel engine the root and mid-flame regions of such a flame may be expected to be in the combustion chamber while the forward section of the flame approaches the cylinder head. The burner is kept in a sealed enclosure. The fuel air mixture ratio is controlled by mass flow controllers (Alborg Instruments and Controls Inc., Orangeburg, USA) fitted to each gas line. The sample collection is controlled automatically by driving three pneumatic cylinders, sequentially, one of which carries a tongue incorporated with a transmission electron microscope (TEM) grid of 3.05 mm diameter and 0.15 mm thickness. This allows control of total sampling time and grid exposure time with millisecond resolution. The burner platform is moved vertically by a stepper motor to allow the collecting tongue to have access to different vertical locations in the flame, h (distance from the flame root).

2.2 Experimental and Analytical Procedures

2.2.1 *Transmission Electron Microscopy Study*

For the TEM study, the soot particles are collected directly on a 200 mesh TEM Cu grid coated with a 10 nm thin carbon layer (Pelco International, A division of Tedpella, Inc. USA). The grids are exposed to the central part of the flame for a few milliseconds for each sampling, at different locations of the central axis of the flame. The location is marked as height, h above the flame root. We also collected particles outside the flame, 8 cm above the flame tip. This position is designated as exhaust.

Structural and other related studies were carried out using two TEMs; (1) the Tecnai F-30 (FEI Inc., USA) is a 300 kV TEM equipped with a Schottky field emission source and a point–point resolution of 2.2 Å and (2) the Tecnai T-20 is a 200 kV TEM with a W-source and an ultra high resolution pole piece with a point–point resolution of 1.9 Å.

HRTEM images were processed using image analysis software ImageJ. The images were digitized and saved in Tiff format of size 1,024 × 1,024, 8 bit, grayscale format. The image was then converted to frequency domain by fast Fourier transform (FFT), where it was filtered through 3.3–4.5 Å bandwidth followed by an inverse FFT of the image. Now, the filtered image was converted into a two phase image by setting a threshold brightness value and then converted to a binary image. The binary image was then further smoothened and eroded. This processed image is considered for fringe analysis. The interplanar spacings (d_{002}) obtained, by refined image analysis and by direct extraction from HRTEM image profile, match well.

2.2.2 *Nanoindentation and Lateral Force Measurement by AFM*

Lateral force measurements (LFMs) were performed in an AFM "Innova" (Veeco, Santa Barbara, USA) using rectangular shaped diamond-like carbon (DLC) coated cantilevers of 5 N/m stiffness (Veeco, Santa Barbara, USA). The radius of the spherical apex of the tip was maintained at approximately 20 nm. SEM and silicon grating imaging were used periodically to check the integrity of the tip radius. The cantilever normal stiffness was calibrated by methods of dimensioning [44] and thermal vibration [45]. All the experiments were done in the ambient. Before the start of each experiment the tip was cleaned in an Ultra Violet chamber (Bioforce Nanoscience, USA) for 15 min.

To enable lateral force study on a single particle the particle needed to be anchored to the substrate. Particles collected from the flame on silicon wafer were suspended in n-hexane (99.9% pure Sigma Aldrich) in a 3% w/v ratio. The suspension was sonicated for 20 min in an ultrasonicator bath. A drop of polymethyl methacrylate (PMMA) (molecular weight of the order of 495,000) dissolved in chloroform ($CHCl_3$, 99% pure, Sigma Aldrich, Mumbai) was poured on a fresh silicon wafer to spin coat the substrate with a rotational speed of 600 rpm. The coating thickness of the PMMA was found to be 10 nm. A drop of the suspension with the particles in it was poured on the coated substrate and spin coated again at 600 rpm. The substrate with the particles is placed in an oven heated to a temperature in the 150–200 °C range. The PMMA melts, when it solidifies the particles are glued to the PMMA layer, the bottom of the particle was found to be in contact with the substrate. The substrate is stored overnight in a dessicator.

For indentation, the particles were collected from the flame after sub-second time exposure, on silicon wafer substrates kept on the tongue located at the end of the collecting arm. The exposure time is maintained as low as possible to avoid overlapping coverage by the particles. The particles on the substrate are stored overnight in a desiccator prior to each experiment. The tapping mode of the AFM was used to image the particle distribution on the silicon wafer. Figure 1 shows such an image of particles collected in the mid-flame region. The imaging was done using a DLC tip of 5 nm radius at 160 Hz frequency.

Indentation experiments were done by programming the indenter to indent at the centre of grids (5 × 6) uniformly located in a 1 mm × 1 mm scan area.

Indentation was performed on particles in the non-imaging mode using a diamond cube corner tip of 40 nm radius, 1,141 GPa Young's modulus and 0.07 Poisson's ratio (Hysitron Triboindenter, Hysitron Inc., Minneapolis, USA). The loading was maintained in the low load range to avoid substrate effect, particle slipping, and particle

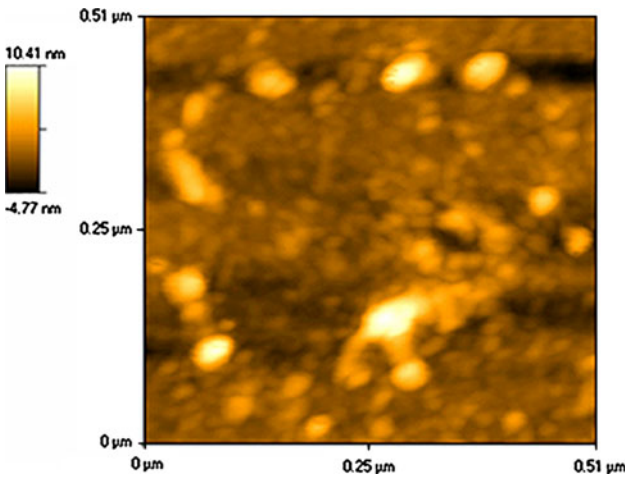

Fig. 1 Tapping mode AFM image of dispersed flame soot particle on silicon substrate

fracture. From the load–displacement curve, hardness was estimated using the built-in software (based on the Oliver and Pharr [46] analysis).

In indenting the grid carrying the soot particles the indenter encounters (a) the silicon substrate, (b) the agglomerates, and (c) the single particle. Figure 2a shows three distinct classes of mechanical responses. To obtain the hardness of single soot particles we discount the substrate and agglomerate data. Separate experiments were done (1) on the silicon wafer which gave hardness in the 10–11 GPa range and (2) on the agglomerates which gave a hardness in the 0.05–0.1 GPa range. We assume that the measured hardness in the 3–5 GPa range is that of single soot particles. Figure 2b shows a typical load–displacement characteristic obtained from a nanoindentation experiment.

The soot single particle hardness data as presented on a relative scale may be acceptable but the single particle hardness data on an absolute scale cannot, however, be accepted with full confidence. For the silicon wafer flat and agglomerated particles ($\approx$1,000–1,500 nm scale) the space indented by an indenter of 40 nm radius may be taken to be semi-infinite spaces and the hardness value may be assumed to be more or less correct. For the single soot particles of 20–40 nm diameters, the 40 nm tip indents to a residual depth of 2–4 nm. Low optical resolution imaging possible in the nanoindenter does not permit clear imaging of an indent. Further it was not possible to locate a nanoindent when the substrate was transferred to an AFM platform. A direct measurement of the contact area of an indent was therefore not possible. Generally up to three particles cluster together on the nanoindenter substrate (Fig. 1). In Appendix 2 we show an image of an indenter of a 1,000 nm diameter agglomerate. The contact area is about 20×10^{-14} m^2 which gives a hardness of about 0.1 GPa, when the indentation load is 20×10^{-6} N. There is thus an undeniable uncertainty in the presented hardness values of the "so called" single particles, compounded by the fact that indentation of a small cluster may involve interparticle slippage, separation of loose particles and slip on the substrate. Young's modulii of the soot particles, deconvoluted using the Oliver and Pharr method [46] from the nanoindentation data showed a large scatter. For the agglomerate (Fig. 2a) the modulus is in the range 7 ± 5 GPa range. For all the other soot, except the one extracted at 5 cm height of the flame, the modulus is 50 ± 15 GPa. A consistent value of 70 ± 15 GPa was obtained for the soot extracted from 5 cm flame height.

2.2.3 Temperature Measurement

For temperature mapping temperature measurement was carried out by a non-contact IR thermometer (Mikron Instrument Company, Inc., USA) placed outside the combustion enclosure and focused through a window opening in the combustion enclosure. The vertical movement of burner with proper delay periods set by the controller was utilized to map temperature of the whole flame along the central axis of the flame.

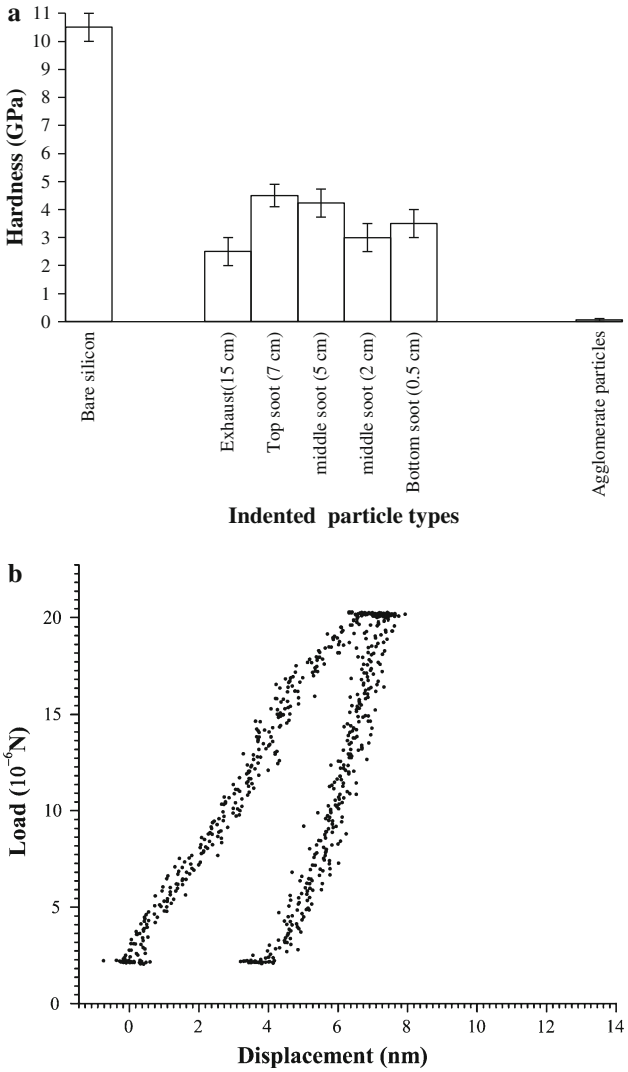

Fig. 2 **a** Hardness of flame soot and bare silicon. **b** A typical load–displacement characteristic of a soot particle ($h = 0.5$ cm) obtained by nanoindentation

3 Results and Discussion

Figure 3 shows the details of a soot particle extracted from the flame. The inset of Fig. 3b gives the FFT image of the particles, the bright spot gives a d spacing of $d_{002} = 0.355$ nm (Fig. 3e), a spacing greater [30–33] than that of ($d = 0.332$ nm) for pure graphite. The data, taken together with the electron diffractogram (Fig. 3d) and XRD

(Fig. 3f) data show the soot to consist of a graphitic outer shell exhibiting short range crystalline order in small but (crystallographically) bent crystallites, roughly parallel and equidistant. Such structure of a shell which has amorphous material as its core has been designated as 'turbostratic graphitic' and has been characterized by others [30–35].

The measured details of the soot morphologies (Fig. 3) correspond well with the reported inter-crystalline spacing [30–33] (Fig. 4a), crystallite length [30, 33] (Fig. 4a), core size [35] (Fig. 4b), and particle size [32, 33, 35–37, 39, 42] (Fig. 4b). We report these parameters as a function of h, where h is the distance of the location from the flame root along the flame central axis.

Figure 4b shows the primary particle to increase in size with h till about $h = 4$ cm; at $h > 4$ cm there is a reduction in primary particle size. This trend has been reported by

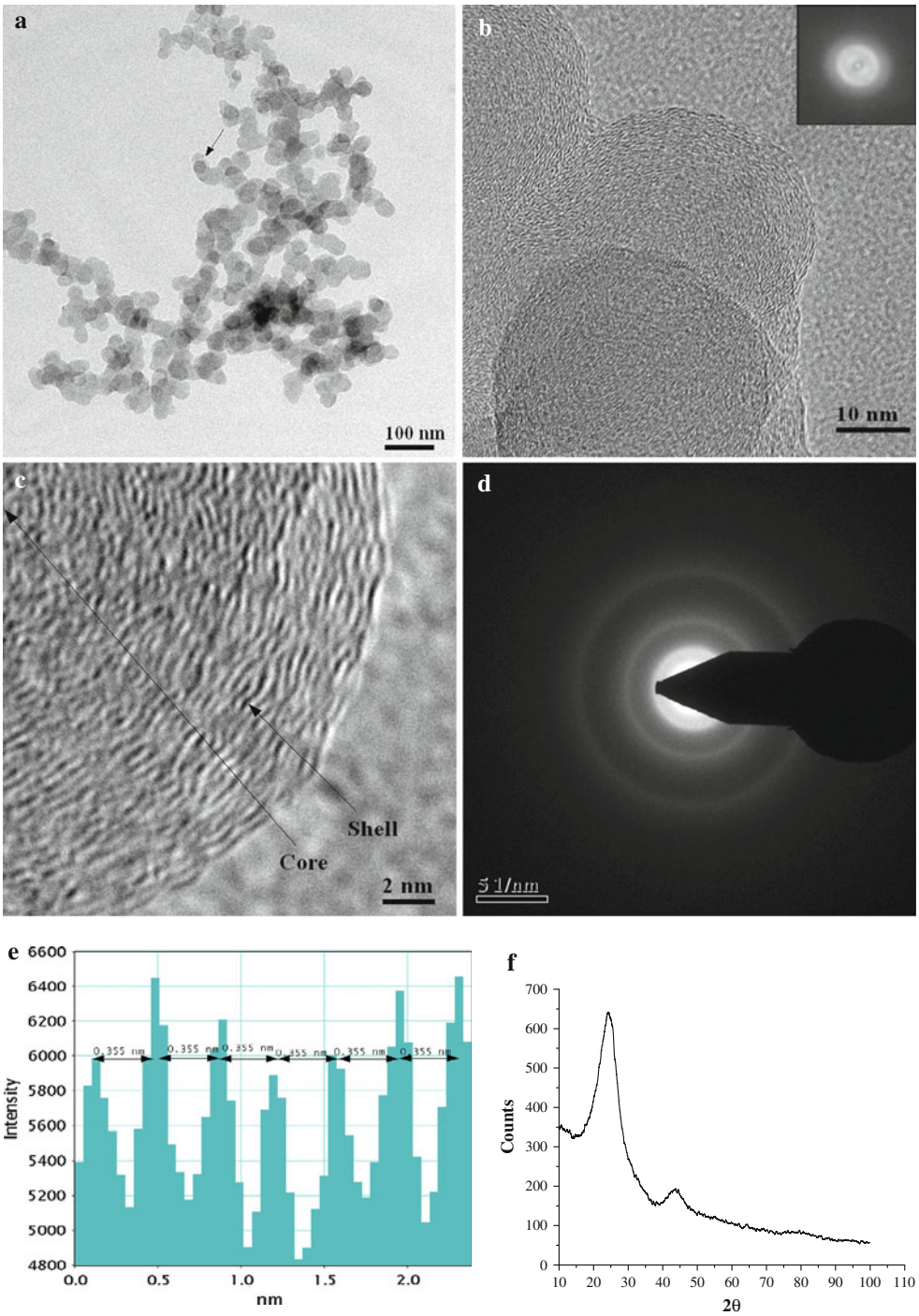

Fig. 3 **a** Low magnification image of particle agglomerate. **b** and **c** HRTEM of the particle marked with a *arrow* in (**a**). **d** Representative selected area electron diffraction of a soot particle. **e** The profile of the regions selected in (**c**), for the extraction of interplanar spacing. **f** XRD of a soot particle ($2\theta = 24.36°$, 43.88° and d spacing = 3.58 Å, 2.06 Å)

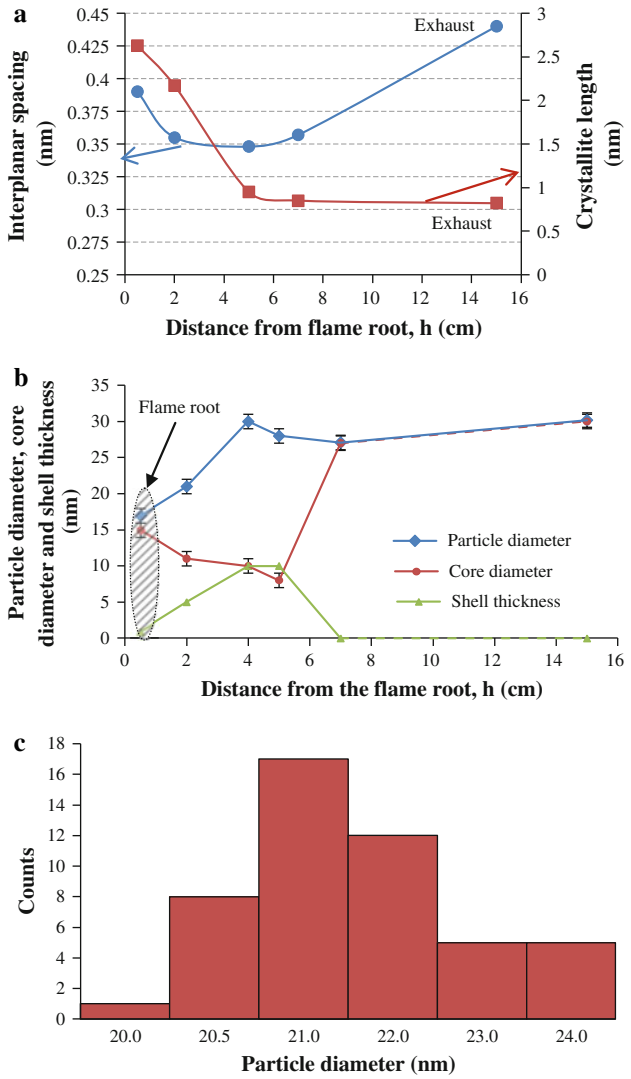

Fig. 4 **a** Variation of average interplanar spacing and crystallite length. **b** Average particle size, core diameter, and shell thickness with height (h) from the flame root, along the flame axis. The *dashed lines* are interpolations along the flame axis. **c** Particle size distribution at 2 cm height along the flame axis, from the flame root

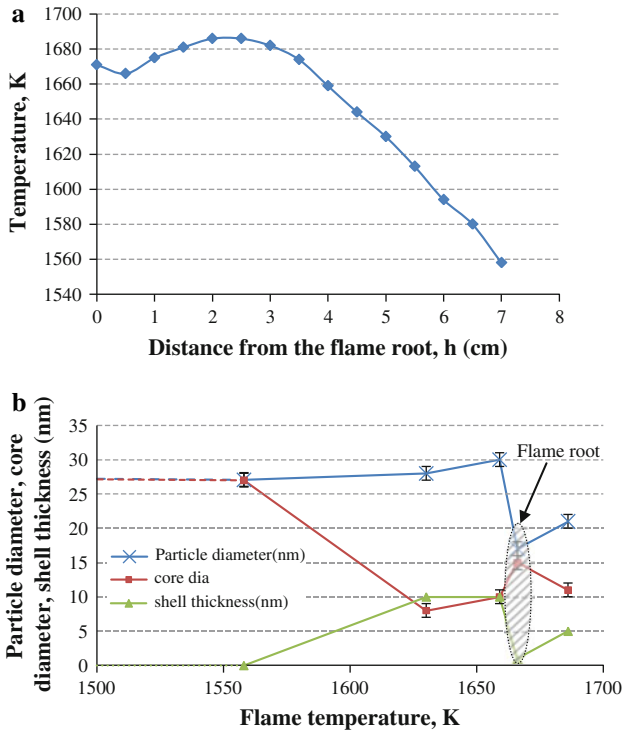

Fig. 5 **a** Measured temperature profile of a flame along the central axis. **b** Average particle size, core diameter, and shell thickness with height (h) from the flame root, along the flame axis. The *dashed lines* are interpolations along the flame axis

others [37, 47]. In soot formation polyaromatic compounds coagulate [48] close to the flame root increasing the particles size with increasing distance away from the root.

Figure 4c shows a typical particle size distribution. While there is growth there is also oxidation which tends to reduce the size. Early work of Dobbins and Megaridis [37], for example, reported an increase in primary particle size till about 40 nm of height above the flame root, followed by a reduction due to oxidation at a longer distance from the flame root. Hurt et al. [49] report a reduction in the size of primary particles with increasing distance from the flame root, due to progressive sintering and collapse.

Figure 4b shows the diameter of the core to reduce consistently with increasing h till $h = 5$ cm. When $h = 7$ cm a distinct central (spherical) core disappears. As the soot moves along the flame axis towards the tip the temperature of the resident zone increases initially and then decreases due to radiative heat transfer. Smooke et al. [48] has underscored the importance of this phenomenon as well as that of the corresponding oxidative increase on the changing chemistry and morphology of soot along the flame axis. Figure 5a shows the variations of temperature along the flame axis, as measured in the present experiments. The trend accords well with that predicted by Smooke et al. [48]. Replotting Fig. 4b on a temperature axis (Fig. 5b) shows the core diameter to decrease from that at the flame root, with increasing temperature in the high temperature zone as well as with decreasing temperature in moving away from the flame root. The latter trend is well explained qualitatively by the equilibrium relations proposed by Hurt et al. [49], where the total free energies of the system consisting of the elastic strain energy and the orientational energy is minimized to give the core radius. The core radius is shown to be inversely proportional to $(T_c - T)$, where T_c is the flame root temperature and T is the temperature at any location along the flame. The following shows that this proportionality breaks down in a small zone above the flame root where the soot is superheated (temperature, more than that of the flame root) but holds further upstream in the subcooled region.

The HRTEM images of the soot particles extracted from the flame often did not allow a clear global demarcation of the crystalline and disordered amorphous phases. The HRTEM image and the extracted pattern of a particle taken at $h = 0.5$ cm (Fig. 6a) shows a very thin ordered shell in a largely amorphous bulk. The soot at this flame root location is the most amorphous in the whole flame (minimum shell thickness) inspite of the fact that the temperature is lower (1,665 K) than that of an upstream superheated region ($h = 2$ cm, temperature = 1,689 K, Fig. 6b). The particle extracted at $h = 2$ cm (Fig. 6b) shows a clear amorphous core surrounded by crystallites arranged radially in columns [49]. Increasing h to 5 cm (subcooled, temperature = 1,657 K) retains the structure (Fig. 6c) but reduces the amorphous core to 6 nm. Figure 6c shows some pockets of disorder also in the shell. Moving further out in the flame ($h = 7$ cm), Fig. 6d, and to the exhaust (Fig. 6e), do not show any distinct core at the centre of the particle but randomly scattered small pockets of disorder surrounded by columnar crystallites.

Fairly soon, after the nucleation stage and in the present case within 5 mm distance from the root, there is an initiation of surface growth which leads to the formation of a crystalline graphitic shell around the disordered coagulated core (Fig. 6b). The particle size growth reaches a limit in the mid-flame region and the size reduces moving towards the tip of the flame. In the reported literature the whole assembly is referred to as a primary particle. It is possible that a reduction of temperature in moving towards the flame tip raises the strain energy of the system to a point where the structure becomes unstable and is forced to reorganize, yielding an altogether new phase.

We believe that the sequence of, core disorder → (long range) ordered shell → ordered/disordered shell → short range order, in the particles that we observe in Fig. 6 with increasing h has a major impact on the mechanical property variation of the soot along its axis.

Figure 7a shows the hardness of single soot particles as a function of temperature. The indent penetration, for $h = 3$, 4, 5 cm particles, was smaller than or the same as the shell thickness (Fig. 6b). For the $h = 0.5$ cm, 7 cm and for the exhaust particles this penetration intruded into the bulk.

We do not have any conclusive explanation for the trend in hardness as seen in Fig. 7a. It is possible that it is simply a bulk thermal effect where increasing temperature brings about lowering of flow stress of the particles, as observed in metals at temperatures above re-crystallization. Figure 7a gives a 50% fall in hardness (from 4.5 to 3 GPa) due to about 150 K increase in temperature, where the flame root temperature is about 1,660 K. That such a large change in bulk hardness is caused by a modest thermal softening of the bulk is a possible but a unlikely explanation.

Field and Swain [50] did spherical indentation on different carbon materials; coke and polycrystalline graphitic and measured hardness values of the order of 3 GPa, a value similar to what is found for the present soot particles. The authors suggest that the deformation of carbon material in indentation is mechanistically controlled by inter-crystalline slip along the basal plane of the graphitic nanocrystals, besides the elastic penetration mechanism. According to this suggestion one would expect particles composed of stacked layers of graphite crystallites to deform easily and yield low hardness compared to that of particles where such mechanism is not available as in this case of amorphous carbon materials.

If there is no bulk thermal softening, according to this model, the flame root soot hardness will be expected to be higher than the hardness of all the upstream particles. In reality it is higher than the hardness of particles collected at the highest temperature but is lower than those of other upstream particles.

Another possible way to rationalize the data is, in terms of stored elastic energy. The formulation of Hurt et al. [49] gives the elastic energy, $G_{\text{elastic}} = C \times E \times s$ where C is a geometric constant, E is Young's modulus and s is the shell thickness (the inner surface of the shell marks the order–disorder phase boundary). By this formulation, when there is an order to disorder phase change, in the present case such a change happens between $h = 2$ and 5 cm (shell thickness between 5 and 10 nm), the elastic energy increases with the thickness of the outer shell of the soot particles. Figure 7b shows an increase in G_{elastic}/C with shell thickness in this range of shell thickness. Hardness indicates resistance to dislocation glide and obstacle to such glide increases the elastic energy of the system and hardness. There is thus a possible correlation between stored elastic energy and hardness where there is a clear order to disorder transition. In the present experiments clear order to disorder transition (Fig. 6b, c) is seen in the 5–10 nm shell thickness range, where the hardness increases with shell thickness (Fig. 7b). The model proposed by Hurt et al. [49] may thus provide a rationale for the hardness variation when there is a clear coexistence of crystalline and disorder phases in a soot particle. The model may not be valid in the 0–4 nm shell thickness range where the amorphous core predominates. Without further corroborative experimental work it is not possible at this stage to conclusively indicate the validity of any or a combination of the above reasonings.

What is interesting in the results presented here is that the friction coefficient of the particles (Fig. 7) averaged over (0.25 μm × 0.25 μm) scan follows roughly the same trend as the hardness up to $h = 7$ cm. Numerical values given in Fig. 7 should be taken with some caution as only a

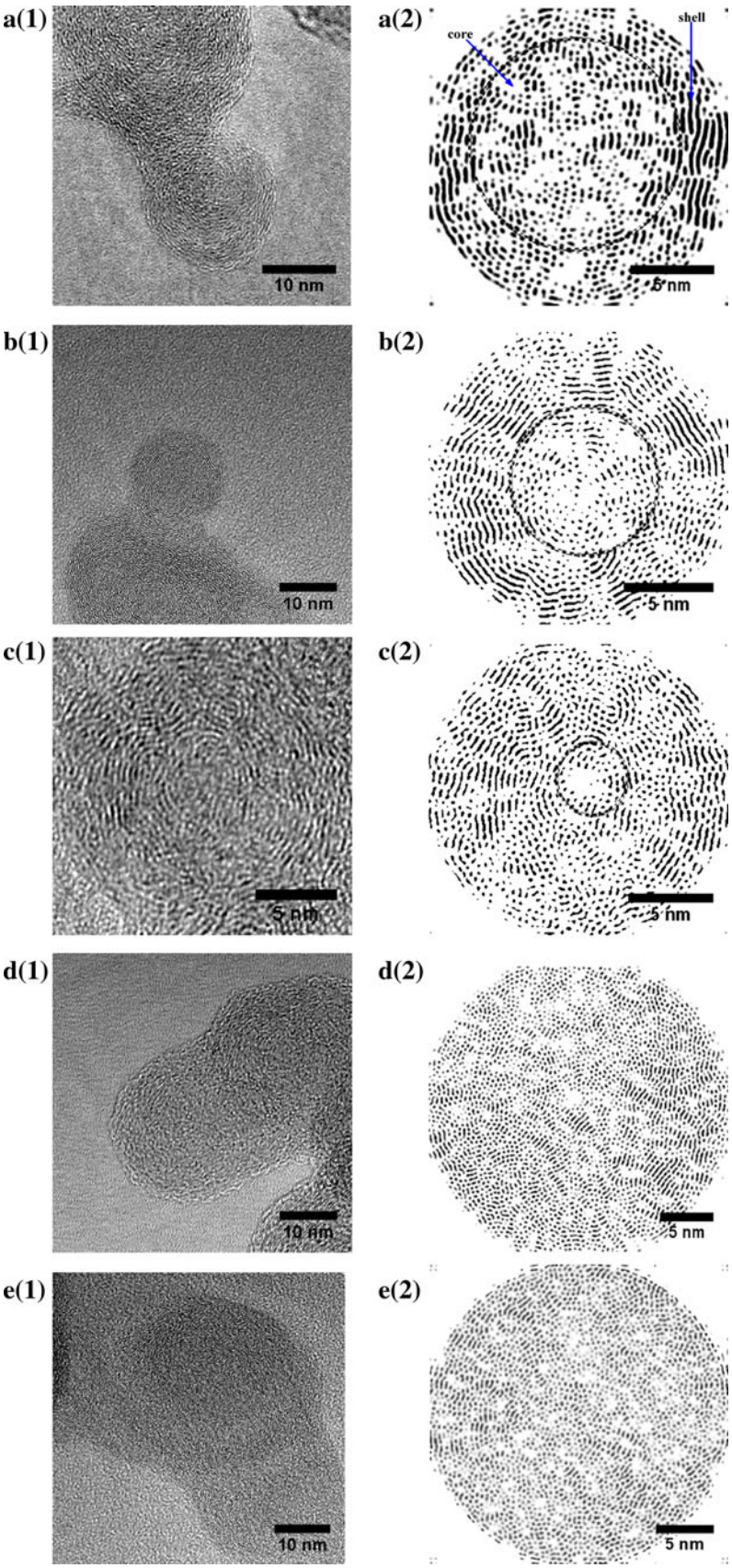

Fig. 6 HRTEM and processed image of soot at **a** 0.5 cm, **b** 2 cm, **c** 5 cm, **d** 7 cm heights from the flame root, and **e** at the exhaust

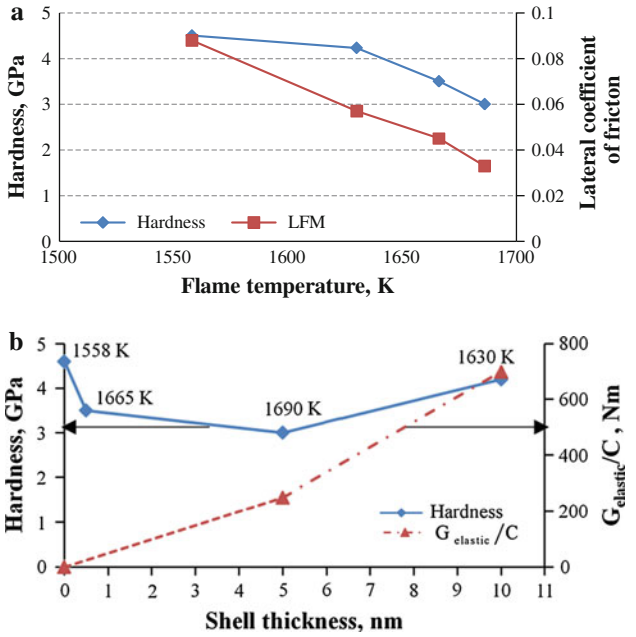

Fig. 7 **a** Hardness and lateral friction coefficient as a function of soot temperature. Peak load for indentation measurement is 20 μN. **b** Variation of hardness with ordered graphitic shell thickness of the particle. *Dashed dotted line* shows the variation of stored elastic energy in a zone where there is an order to disorder transition. The estimate, where C is a geometric constant, is as per the formulation of Hurt et al. [49]

very few out of a large number of trails gave consistent results.

If we estimate a shear strength value τ, as $\tau = \frac{\mu N}{A}$, where μ is coefficient of friction, N (=300 nN) is the normal load and A is the scan area, the value of τ, with reference to Fig. 7a varies in the 0.15–0.45 MPa range. The isotropic shear strength τ_i approximately calculated from the hardness data $\tau_i \approx \frac{H}{6}$ varies in the 0.5–0.75 GPa range. This difference of magnitude by a factor of three suggests that the soot material is layered and the tangential force applied on the layer plane is resisted by a weak interplanar bond.

In a previous paper [51] we had proposed a model, based on mode II fracture mechanics, for a layered material removal process by LFM scanning. The model was validated for layered MoS_2 single particles by demonstrating that the thickness of removed material increases monotonically with applied normal load. A similar experiment done here with a single (it may be 2 or 3 agglomerated particles) soot particles gave a similar thickness of material removal versus normal load characteristic as seen in Fig. 8a. This suggests that the soot material on the application of a lateral force is removed in layers. If this phenomenon is indeed true one would expect the soot with a pronounced graphitic layered shell structure (Fig. 3b) to be more prone to material removal than one which mainly consists of a disordered amorphous core (Fig. 6a, d, e). Figure 8b shows the material removal is indeed greatest when the soot has a thick ordered shell and least when it has a pronounced disordered core (flame root and tip).

The present results show that the normal and shear strengths of soot increases as the particle becomes more disordered. The short range ordered structure of the soot particle at the flame tip and the exhaust promotes a great enhancement of mechanical properties over those corresponding to the other parts of the flame. This enhancement on the one hand protects the soot but may be held, on the other hand, responsible for abrasion of tribological components when soot is inducted into at such contacts, suspended in oil.

The range of soot hardness (3–5 GPa) obtained here is less than the range of hardness met in industrial cast iron engine liners and piston materials which is of the order of Brinell 700 or Rockwell C 63 (or equivalent 5–7 GPa) [52]. On a rule of thumb basis one may not expect the present soot particles to be capable of abrading the liners. For comparison we used the present method to indent particles extracted from the circulating lubricating oil of an industrial diesel engine (as supplied to us by Indian Oil Corporation (R&D), Faridabad, India). The hardness of the industrial soot was found to be about 6 GPa (standard deviation, $\sigma = \pm 1.5$ GPa) a hardness close to what is reported by other [53]. Such particles are likely to abrade a

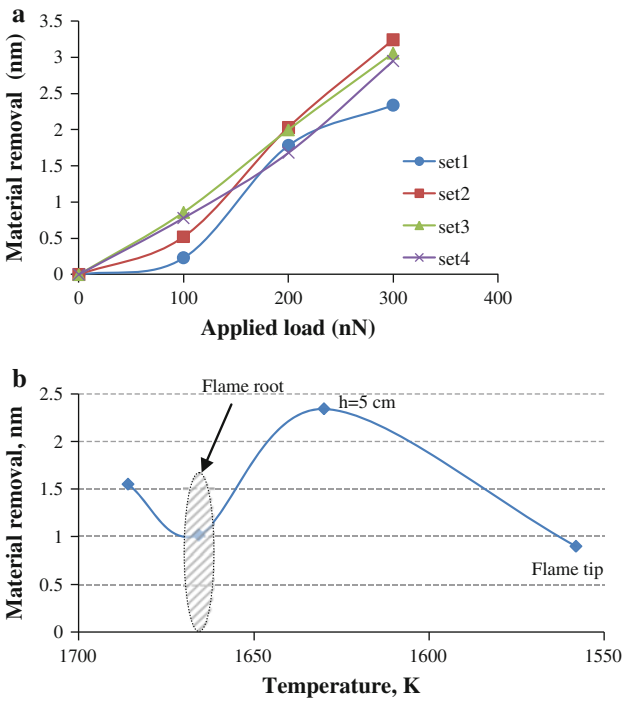

Fig. 8 **a** Soot material removal in the LFM as a function of normal load, showing typical data scatter, $h = 5$ cm. **b** Material removal as a function of soot temperature, normal load = 300 nN

cast iron liner. We suggest that the hardness recorded here for this laboratory soot is low in comparison with that of the industrial soot because here a purely gaseous fuel is used to generate soot, whereas the combustion flame in an engine is made by burning liquid industrial fuel and the byproduct is hard soot.

4 Conclusions

Thermophoretically sampled soot at different locations of a flame generated by burning ethylene gas are found to have widely different morphologies and crystallographic orders. Moving up in the flame from the root, surface growth occurs over the disordered core yielding a large shell of crystalline flakes which organize themselves in a columnar stack positioned radially. Moving towards the flame tip and above the flame the crystalline and amorphous materials in the soot break up and the fragments are reorganized in a randomly distributed space where nanometric size amorphous islands are surrounded by stacks of very small crystalline flakes. The hardness, friction, and resistance to material removal of this phase, present near the flame tip and the exhaust are high. Such properties of the strongly ordered soot extracted from the mid-flame region are comparatively low.

Acknowledgments The authors are grateful to the Indian Oil Corporation Limited (R&D), Faridabad for the financial support which has made this work possible. The authors are also grateful to Dr. S.K. Majumdar of Indian Oil Corporation Limited (R&D) for initiating them to the problem of diesel soot tribology.

Appendix 1

Thermophoretic Sampling

Thermophoretic sampling of soot from the flame generated in the laboratory has been an important tool for researches into soot [37–43]. The thermophoretic sampling method was first developed by Dobbins and Megaridis [37]. Hurd and Flower [38] devised a retractable sheath to protect the grid while the probe was inserted into the desired position in the flame. Köylü et al. [39] fabricated grids attached to a circular recess at the tip of a stainless steel substrate that was rapidly inserted into the flame using a double-acting pneumatic cylinder. Sorensen et al. [40] used a "frog-tonge" probe device, designed after Dobbins and Megaridis's system. This device injects the grids into the flame for a residence time of 15 ms and grids were held with their faces in the vertical plane (parallel to the flame gas flow). Recently, Choi and co-workers [43] analyzed the flow disturbance in the flame caused by the probe's motion. Their design also involved grid cover to avoid the exposure of flame and they used two pneumatic cylinders for translation.

Appendix 2

See Fig. 9.

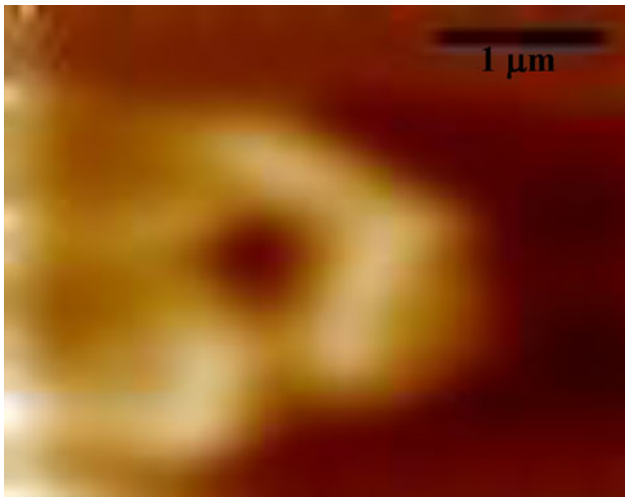

Fig. 9 Image of an indent of an agglomerate of approximately 1,000 nm size, as imaged in the nanoindenter

References

1. Rounds, F.G.: Carbon: cause of diesel engine wear? SAE Prepr. 770829 (1977)
2. Green, D.A., Lewis, R., Dwyer-Joyce, R.S.: Wear effects and mechanisms of soot-contaminated automotive lubricants. Proc. Inst. Mech. Eng. J. **220**, 159–169 (2006)
3. Ramkumar, P., Wang, L., Harvey, T.J., Wood, R.J.K., Nelson, K., Yamaguchi, E.S., Harrison, J.J., Powrie, H.E.G.: The effect of diesel engine oil contamination on friction and wear. In: Proceedings of the World Tribology Congress III, pp. 537–538 (2005)
4. Yamaguchi, E.S., Untermann, M., Roby, S.H., Ryason, P.R., Yeh, S.W.: Soot wear in diesel engines. Proc. Inst. Mech. Eng. J. **220**, 463–469 (2006)
5. Nagai, I., Endo, H., Nakamura, H., Yano, H.: Soot and valve train wear in passenger car diesel engines. SAE Spec. Publ. 87–101 (1983)
6. Yoshida, K., Sakurai, T.: Mechanism of valve train wear caused by diesel soot. J. Jpn. Soc. Lubr. Eng. Int. Ed. **10**, 99–104 (1989)
7. Rounds, F.G.: Generation of synthetic diesel engine oil soots for wear studies. Lubr. Eng. **40**, 394–401 (1984)
8. Berbezier, I., Martin, J.M., Kapsa, Ph.: The role of carbon in lubricated mild wear. Tribol. Int. **19**, 115–122 (1986)
9. Ryason, P.R., Hansen, T.P.: Voluminosity of soot aggregates. A means of characterizing soot-laden oils. SAE Trans. **100**, 897–903 (1991)
10. Rounds, F.G.: Soots from used diesel engine oils—their effects on wear as measured in 4-ball wear tests. SAE Prepr. 810499 (1981)

11. Antusch, S., Dienwiebel, M., Nold, E., Albers, P., Spicher, U., Scherge, M.: On the tribochemical action of engine soot. Wear **269**, 1–12 (2010)
12. Soejima, M., Ejima, Y., Uemori, K., Kawasaki, M.: Studies on friction and wear characteristics of cam and follower: influences of soot contamination in engine oil. JSAE Rev. **23**, 113–119 (2002)
13. Kuo, C.C., Passut, C.A., Jao, T.C., Csontos, A.A., Howe, J.M.: Wear mechanism in Cummins M-11 high soot diesel test engines. SAE Spec. Publ. **1368**, 21–32 (1998)
14. Gautam, M., Durbha, M., Chitoor, K., Jaraiedi, M., Mariwalla, N., Ripple, D.: Contribution of soot contaminated oils to wear. SAE Spec. Publ. **1372**, 55–67 (1998)
15. Gautam, M., Chitoor, K., Durbha, M., Summers, J.C.: Effect of diesel soot contaminated oil on engine wear-investigation of novel oil formulations. Tribol. Int. **32**, 687–699 (1999)
16. Ryason, P.R., Chan, I.Y., Gilmore, J.T.: Polishing wear by soot. Wear **137**, 15–24 (1990)
17. Chinas-Castillo, F., Spikes, H.A.: The behavior of diluted sooted oils in lubricated contacts. Tribol. Lett. **16**, 317–322 (2004)
18. Hosonuma, K., Yoshida, K., Matsunaga, A.: The decomposition products of zinc dialkyldithiophosphate in an engine and their interaction with diesel soot. Wear **103**, 297–309 (1985)
19. Papay, A.G.: Antiwear and extreme pressure additives in lubricants. Lubr. Sci. **10**, 208–224 (1998)
20. Chinas-Castillo, F., Spikes, H.A.: The behavior of colloidal solid particles in elastohydrodynamic contacts. Tribol. Trans. **43**, 387–394 (2000)
21. Mainwaring, R.: Soot and wear in heavy duty diesel engines. SAE paper 971631 (1997)
22. Covitch, M.J., Humphrey, B.K., Ripple, D.E.: Oil thickening in the Mack t-7 engine test—fuel effects and the influence of lubricant additives on soot aggregation. SAE Spec. Publ. 65–80 (1985)
23. Kim, C., Passut, C.A., Zang, D.M.: Relationships among oil composition combustion-generated soot, and diesel engine valve train wear. SAE 922199 (1992)
24. Corso, S., Adamo, R.: Effect of diesel soot on reactivity of oil additives and valve train materials. SAE Spec. Publ. 41–55 (1984)
25. Querlioza, E., Ville, F., Lenon, H., Lubrecht, T.: Experimental investigations on the contact fatigue life under starved conditions. Tribol. Int. **40**, 1619–1626 (2007)
26. Colacicco, P., Mazuyer, D.: The role of soot aggregation on the lubrication of diesel engine. Tribol. Trans. **38**, 959–965 (1995)
27. Kleiser, W., Walker, H., Rutherford, J.: Determination of lubricating oil additive effects in taxicab service. SAE Tech. Paper 912386 (1991)
28. Tree, D.R., Svensson, K.I.: Soot processes in compression ignition engines. Prog. Energy Combust. Sci. **33**, 272–309 (2007)
29. Liu, C., Nemoto, S., Ogano, S.: Effect of soot properties in diesel engine oils on frictional characteristics. Tribol. Trans. **46**, 12–18 (2003)
30. Palotas, A.B., Rainey, L.C., Feldermann, C.J., Sarofim, A.F., Vander Sande, J.B.: Soot morphology: an application of image analysis in high-resolution transmission electron microscopy. Microsc. Res. Tech. **33**, 266–278 (1996)
31. Zhu, W., Miser, D.E., Chan, W.G., Hajaligol, M.R.: Characterization of combustion fullerene soot, C_{60}, and mixed fullerene. Carbon **42**, 1463–1471 (2004)
32. Chen, Y., Shah, N., Braun, A., Huggins, F.E., Huffman, G.P.: Electron microscopy investigation of carbonaceous particulate matter generated by combustion of fossil fuels. Energy Fuels **19**, 1644–1651 (2005)
33. Wentzel, M., Gorzawski, H., Naumann, K.H., Saathoff, H., Weinbruch, S.: Transmission electron microscopical and aerosol dynamical characterization of soot aerosols. J. Aerosol Sci. **34**, 1347–1370 (2003)
34. Song, J., Alam, M., Boehman, A.L.: Characterization of diesel and biodiesel soot. Am. Chem. Soc. Div. Fuel Chem. **49**, 767–769 (2004)
35. Ishiguro, T., Takatori, Y., Akihama, K.: Microstructure of diesel soot particles probed by electron microscopy: first observation of inner core and outer shell. Combust. Flame **108**, 231–234 (1997)
36. Santoro, R.J., Semerjian, H.G.: Soot formation in diffusion flames: flow rate, fuel species and temperature effects. Int. Symp. Combust. **20**, 997–1006 (1984)
37. Dobbins, R.A., Megaridis, C.M.: Morphology of flame-generated soot as determined by thermophoretic sampling. Langmuir **3**, 254–259 (1987)
38. Hurd, A.J., Flower, W.L.: In situ growth and structure of fractal silica aggregates in a flame. J. Colloid Interface Sci. **122**, 178–192 (1988)
39. Köylü, Ü.Ö., McEnally, C.S., Rosner, D.E., Pfefferle, L.D.: Simultaneous measurements of soot volume fraction and particle size/microstructure in flames using a thermophoretic sampling technique. Combust. Flame **110**, 494–507 (1997)
40. Sorensen, C.M., Feke, G.D.: The morphology of macroscopic soot. Aerosol Sci. Technol. **25**, 328–337 (1996)
41. Cai, J., Lu, N., Sorensen, C.M.: Comparison of size and morphology of soot aggregates as determined by light scattering and electron microscope analysis. Langmuir **9**, 2861–2867 (1993)
42. Frank, E.K., Wim, O., Jan, M., Joop, S., Brian, S.: Particle formation paths in the synthesis 2 of silicon nitride powder in a laser-heated aerosol reactor. J. Eur. Ceram. Soc. **18**, 1025–1036 (1998)
43. Lee, J., Altman, I., Choi, M.: Design of thermophoretic probe for precise particle sampling. J. Aerosol Sci. **39**, 418–431 (2008)
44. Cleveland, J.P., Manne, S., Bocek, D., Hansma, P.K.: A nondestructive method for determining the spring constant of cantilevers for scanning force microscopy. Rev. Sci. Instrum. **64**, 403–405 (1993)
45. Hutter, J.L., Bechhoefer, J.: Calibration of atomic-force microscope tips. Rev. Sci. Instrum. **64**, 1868–1873 (1993)
46. Oliver, W.C., Pharr, G.M.: An improved technique for determining hardness and elastic modulus using load and displacement sensing indentation experiments. J. Mater. Res. **7**, 1564–1583 (1992)
47. Sunderland, P.B., Faeth, G.M.: Soot formation in hydrocarbon/air laminar jet diffusion flames. Combust. Flame **105**, 132–146 (1996)
48. Smooke, M.D., Long, M.B., Connelly, B.C., Colket, M.B., Hall, R.J.: Soot formation in laminar diffusion flames. Combust. Flame **143**, 613–628 (2005)
49. Hurt, R.H., Crawford, G.P., Shim, H.S.: Equilibrium nanostructure of primary soot particles. Int. Symp. Combust. **28**, 2539–2546 (2000)
50. Field, J.S., Swain, M.V.: The indentation characterization of the mechanical properties of various carbon materials: glassy carbon, coke and pyrolytic graphite. Carbon **34**, 1357–1366 (1996)
51. Sahoo, R.R., Math, S., Biswas, S.K.: Mechanics of deformation under traction and friction of a micrometric monolithic MoS_2 particle in comparison with those of an agglomerate of nanometric MoS_2 particles. Tribol. Lett. **37**, 239–249 (2010)
52. Taylor, C.F.: The Internal-Combustion Engine in Theory and Practice: Combustion, Fuels, Materials, Design, vol. 2: Revised edn., pp. 341–342. MIT Press, USA (1985)
53. Jap, T.C., Li, S., Yatsunami, K., Chen, S.J., Csontos, A.A., Howe, J.M.: Soot characterisation and diesel engine wear. Lubr. Sci. **16**, 111–126 (2004)